Journal of Applied Fluid Mechanics, Vol. 17, No. 9, pp. 2028-2044, 2024.
Available online at www.jafmonline.net, ISSN 1735-3572, EISSN 1735-3645.
https://doi.org/10.47176/jafm.17.9.2631

A Comparative Assessment of Various Cavitator Shapes for High-speed Supercavitating Torpedoes: Geometry, Flow-physics and Drag Considerations

K. Gaurav, N. Venkatesh and A. Karn†

Department of Aerospace Engineering, Mechanical Cluster, School of Advanced Engineering, UPES, Dehradun, Uttarakhand, 248007, India

†Corresponding Author Email: akarn@ddn.upes.ac.in

ABSTRACT

Modern underwater warfare necessitates the development of high-speed supercavitating torpedoes. Achieving supercavitation involves integrating a cavitator at the torpedo's front, making cavitator design a critical research area. The present study simulated supercavity formation by cavitators of various shapes attached to a heavyweight torpedo. The study involves simulations of thirteen cavitator designs with various geometrical configurations at different cavitation numbers. The simulations employ the VOF multiphase model along with the Schnerr and Sauer cavitation model to analyze supercavitation hydrodynamics. The study examines the supercavity geometry and drag characteristics for individual cavitator designs. The results reveal a significant reduction in skin friction drag by a majority of cavitators. Notably, a disc cavitator at a cavitation number of 0.09 demonstrates a remarkable 92% reduction in the coefficient of skin friction drag. However, the overall drag reduces when incorporating a cavitator, but it introduces additional pressure drag. The study found that the cavitators generating larger supercavities also yield higher pressure drag. Therefore, the supercavity should just envelop the entire torpedo, as excessively small supercavities amplify skin friction drag, while overly large ones elevate pressure drag. Ultimately, the study concludes that selecting the ideal cavitator entails a comprehensive evaluation of factors such as supercavity and torpedo geometry, reductions in skin friction drag and increments in pressure drag.

Article History

Received January 29, 2024
Revised April 10, 2024
Accepted April 13, 2024
Available online July 2, 2024

Keywords:

Multiphase flow
Supercavitation simulation
Flow control
Drag reduction
Under-water vehicle
SS cavitation model
Shape optimization

1. INTRODUCTION

Supercavitation is a hydrodynamic phenomenon that involves the formation of a large gaseous cavity around an object moving through a liquid medium (Oba et al., 1980; Cao et al., 2017). This supercavity reduces the skin friction drag on the object, allowing it to move faster and more efficiently through the water (Savchenko, 2001). Supercavitation can be accomplished through two distinct methods: the natural approach, commonly identified as vaporous supercavitation, and the artificial method, often referred to as ventilated supercavitation (Zhang et al., 2007; Karn & Rosiejka, 2017). When the velocity of the body is high enough to create a drop in ambient pressure close to the vapour pressure of the surrounding liquid, a phase transition occurs, and the liquid turns into vapor. This phenomenon is known as natural supercavitation and it leads to the formation of a vaporous enclosure around a body (Shi et al., 2000; Nesteruk, 2012). Conversely, the artificial technique of supercavitation involves the injection of a non-condensable gas at the nose of the underwater vehicle, resulting in the formation of the supercavity (Semenenko, 2001; Karn et al., 2016a). In the case of artificial supercavitation, the formation and coalescence properties of gas bubbles play a crucial role in predicting the geometry of the supercavity (Gaurav et al., 2022; Karn et al., 2016b). Notably, achieving artificial supercavitation necessitates lower velocities compared to those required for the attainment of natural supercavitation (Javadpour et al., 2017; Shao et al., 2017).

The principle of supercavitation has been investigated for various applications such as underwater transport, desalination, aeration, waste water treatment etc. (Schmid, 2009; Likhachev et al., 2014; Karn et al., 2015b; Sarc et al., 2018; Kosel et al., 2020). Supercavitation holds a crucial application in the field of supercavitating

NOMENCLATURE

CC-120	conical cavitator with cone angle of 120^0	*MC-2*	cavitator designed for minimum drag using Eq. 1 (Myring, 1976), $n = 2$.
CC-90	conical cavitator with cone angle of 90^0	*NC*	No Cavitator
CC-60	conical cavitator with cone angle of 60^0	*PC*	Parabolic Cavitator
DC	Disc Cavitator	*SC*	Spherical Cavitator
EC	Elliptical Cavitator	*TC-16*	truncated cone cavitator with a/b value of approximately 16%
MC-1	cavitator designed for minimum drag using Eq. 1 (Myring, 1976), $n = 1$.	*TC-32*	truncated cone cavitator with a/b value of approximately 32%
MC-1.5	cavitator designed for minimum drag using Eq. 1 (Myring, 1976), n = 1.5.	*TC-48*	truncated cone cavitator with a/b value of approximately 48%

torpedoes, which can travel at extremely high speeds underwater by utilizing the reduced drag offered by the supercavity. (Choi et al., 2005; Karn et al., 2015a). These torpedoes typically have a specially designed nose cone (cavitator) that initiates the cavitation process and maintains the supercavity (Ahn et al., 2017; Rajkumar et al., 2023).

A cavitator serves a crucial role in the functioning of supercavitation vehicles. It is a hydrodynamic device intended to initiate and maintain the formation of a supercavity around an underwater vehicle travelling at high speeds (Park & Rhee, 2012). A careful design of the cavitator is imperative to achieve and maintain supercavitation effectively (Xu & Khoo, 2020). The shape of the cavitator is optimized to create a zone of low pressure around the vehicle as it moves through the water. The decrease in pressure triggers the vaporization of the liquid and thus facilitates the development and growth of the supercavity (Mokhtarzadeh et al., 2012). A. Substantial research has been carried out to comprehend the effect of cavitator shape on supercavitation characteristics. Semenenko (2001) specifically used findings from experiments to establish semi-empirical formulations for drag coefficients for disc- and cone-shaped cavitators (Semenenko, 2001). Ahn et al. (2010) examined the variation of supercavity dimensions for wedge and cone cavitators under various ventilation and flow circumstances (Ahn et al., 2010). They demonstrated specifically that, as compared to a disc cavitator with the same frontal area, cone and wedge cavitators produce a shorter and slimmer cavity (Newman, 2018). Efforts have been made in the past to investigate the effect of cavitator shape on the ventilation demand to form and sustain a ventilated supercavity under different flow conditions and it has been reported that the cone-shaped cavitator requires the least amount of ventilation to generate a supercavity among all different shapes across the wide range of Froude number (Shao et al., 2020).

Apart from the capability of the cavitator to generate larger supercavities, a lot of research has been conducted on the drag characteristics of various cavitator shapes. For instance, the experiments by Moghimi et al. (2017) compared disc, cone, and parabolic cavitators for the corresponding cavity dimensions, and overall drag reduction effect at various cavitation numbers. The results indicate that the parabolic cavitator reduces drag the least of the three cavitators with the same frontal area (Moghimi et al., 2017). Using an elliptical disk-shaped cavitator has been shown to increase underwater vehicle performance by lowering drag, according to previous studies. However, maintaining the supercavitating state requires a higher speed compared to other cavitators, such as disc and cone-shaped cavitators (Chen et al., 2023). Researchers have also investigated the effects of holes in the disc cavitator on the cavitation flow at extremely low cavitation numbers. The addition of a concentric hole with various diameters to the disc cavitator affects the cavity features and the degree of drag reduction at various cavitation numbers (Erfanian & Anbarsooz, 2018).

A substantial amount of investigation has been carried out in this particular field. However, the majority of the studies have primarily focused only on the geometrical features of the supercavity generated by various cavitators rather than the drag characteristics. Additionally, most earlier studies focused on just a few geometries (namely, disc and conical) when designing cavitators. Furthermore, the experimental investigations mounted cavitators using strut rather to the actual scenario where cavitators are attached to the torpedo. As a result, the reduction in skin friction drag caused by the supercavitation could not be estimated in the earlier research. Due to this restriction, it is challenging to select an appropriate cavitator for a particular vehicle because data on the net change in drag is not readily available. This paper explores various properties of different cavitator shapes specifically for a heavy-weight torpedo and hence enable us to estimate the reduction in skin friction drag resulting from the supercavity formed around the torpedo. The article presents a comprehensive study of various cavitator shapes, considering the geometrical parameters of the supercavity, the increase in pressure drag, and the decrease in skin friction drag.

Section 2 outlines the methodological approach employed for the current investigation. Subsections 2.1, 2.2, 2.3 and 2.4 elaborate on the torpedo and cavitator geometries, mesh properties, computational methods, and validation of numerical model respectively. Moving forward, Section 3 presents the computational findings and their corresponding discussions based on extensive analysis. Section 4 provides a conclusion summary of the study.

2. METHODOLOGY

The current study involves conducting simulations on fourteen distinct geometries. Specifically, one of these

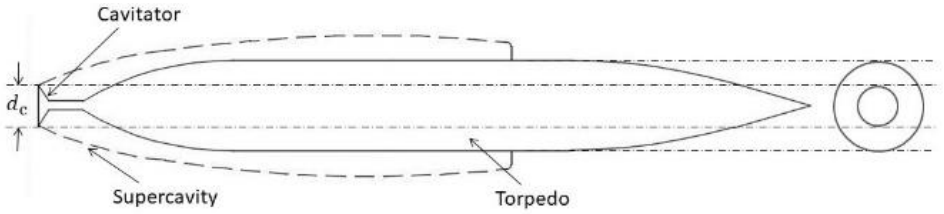

Fig. 1 Geometrical features of torpedo with a cavitator attached at the front

geometries is a torpedo without a cavitator, while the remaining thirteen geometries have different cavitator shapes. The cavitator shapes utilized in this research are as follows: a disc cavitator (DC), three conical cavitators (CC-120, CC-90, and CC-60), three tapered cone cavitators (TC-0.16, TC-0.31, and TC-0.47), an elliptical cavitator (EC), a parabolic cavitator (PC), a spherical cavitator (SC), and three Myring cavitators (MC-1, MC-1.5, and MC-2). For natural supercavitation, the cavitation number is calculated as $\sigma_c = (p - p_v)/0.5\rho V^2$, where p_v is the vapour pressure of the liquid; p, ρ and V are the static pressure, density, and velocity of the freestream flow respectively. Each of these geometries undergoes testing at five distinct cavitation numbers, ranging from 0.092 to 0.128. The corresponding Reynolds number of the flow is calculated based on the cavitator diameter (d_c) as $Re = \rho V d_c/\mu$, where μ denotes the dynamic viscosity of the freestream flow. The simulations in this study are carried out at Reynolds number ranging from $2\,X\,10^7$ to $2.3\,X\,10^7$. Consequently, the study comprises a total of 70 distinct simulations.

2.1 Geometry

A survey of numerous heavy-weight torpedoes is conducted to select the torpedo's geometry for the present study. Majority of the torpedoes are considered from India, Russia, UK, and USA. The torpedo design employed in the current study has a length of 8 metres and a diameter of 800 millimetres. The equation for designing the torpedo for minimum drag is derived by Myring (1976). The equation for designing nose and tail of the torpedo is shown in Eqs. (1) and (2) respectively. The main body of the torpedo is considered to be of cylindrical shape. In the present study same approach is used to design the torpedo

$$y_n = \frac{1}{2} d \left[1 - \left(\frac{x-a}{a}\right)^2\right]^{1/n} \tag{1}$$

$$y_t = \frac{1}{2} d - \left(\frac{3d}{2c^2} - \frac{tan\theta}{c}\right)(x - a - b)^2 + \left(\frac{d}{c^3} - \frac{tan\theta}{c^2}\right)(x - a - b)^3 \tag{2}$$

where y_n and y_t are y locations of nose and tail curve respectively, a, b and c are the length of the nose, main body and tail of the torpedo respectively, d is the maximum diameter of the torpedo, θ is the half-angle made by the tail as illustrated in Fig 1. The bluntness of the nose is governed by the variable n, larger values of n result in a highly blunted nose. The cavitator is attached to the torpedo's nose by a 150 mm-long circular rod to generate supercavity as shown in Fig 1.

In the present work, seven different cavitator shapes i.e., a disc cavitator (DC), conical cavitator (CC), tapered cone cavitator (TC), an elliptical cavitator (EC), a parabolic cavitator (PC), a spherical cavitator (SC), and Myring cavitator (MC) are employed to generate a supercavity on the torpedo. The diameter of all the cavitators (d_c) is kept constant i.e., 320 mm in the present study. Figure 2 shows the shapes of these cavitators.

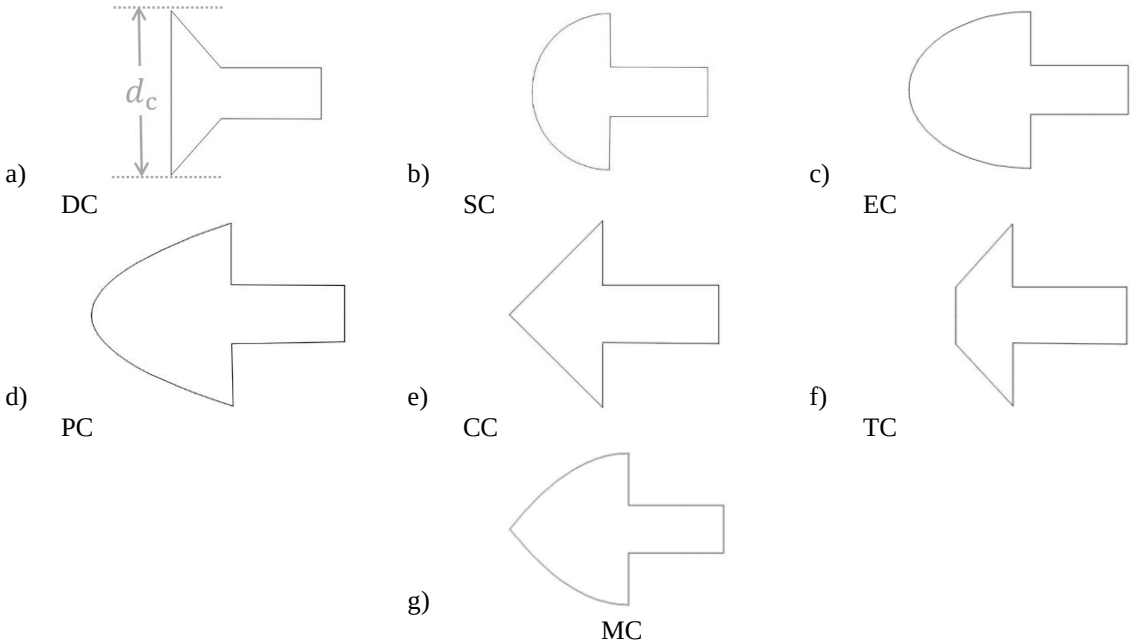

Fig. 2 Shape of various cavitator used in present study: (a) Disc Cavitator, (b) Spherical Cavitator, (c) Elliptical Cavitator, (d) Parabolic Cavitator, (e) Conical Cavitator, (f) Tapered Cone Cavitator and (g) Myring Cavitator

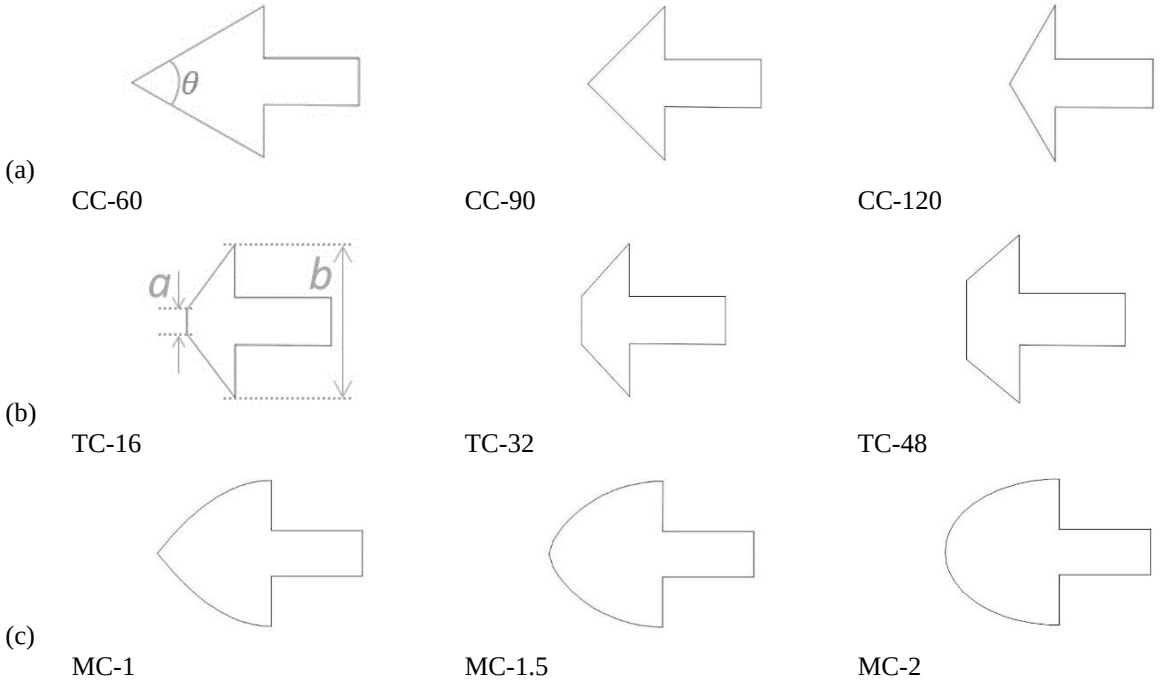

Fig. 3 Various geometrical configurations of (a) Conical Cavitators (CC), (b) Tapered Cone Cavitators (TC), and (c) Myring Cavitators (MC) used in the present study

Table 1 Properties of meshes used for grid independence test

Mesh	No. of elements	Wall Distance	Y+ Value
Mesh-1	40,000	$6.1\ X\ 10^{-5}\ m$	150
Mesh-2	56,000	$4.1\ X\ 10^{-5}$m	100
Mesh-3	80,000	$1.6\ X\ 10^{-5}m$	40
Mesh-4	112,000	$8.2\ X\ 10^{-6}m$	20

Three different geometrical configurations are used in the case of conical, tapered cone and Myring cavitator shape, Distinct cone angles (θ) are used to design conical cavitators; CC-120, CC-90, and CC-60 (Fig. 3a), respectively, have cone angles of 120º, 90º, and 60º. As illustrated in Fig 3b, varied ratios between the tapered diameter (a) and base diameter (b) are used to design tapered cone cavitators; TC-16, TC-32, and TC-48 have, respectively, a/b ratios of 16%, 32%, and 48%. Myring cavitators (Fig. 3c) are designed to offer low pressure drag using Eqn. 1. Three different values of n are adopted for the design of the Myring cavitators; the n values for the MC-1, MC-1.5, and MC-2 are 1, 1.5, and 2 respectively.

2.2 Meshing

To finalize the mesh for the present study, a grid independence test is conducted using four structured meshes with different numbers of elements. The first mesh, referred to as Mesh-1, contains around 40,000 elements. For the second mesh (Mesh-2), the number of elements is increased by 1.4, resulting in approximately 56,000 elements. Similarly, the third mesh (Mesh-3), and fourth mesh (Mesh-4) contain 80,000 and 112,000 elements, respectively. The details of all the meshes are tabulated in Table 1.

The simulation is conducted at five different cavitation numbers ranging from 0.09 to 0.13 on a torpedo with a conical cavitator having a diameter of 120mm (CC-120). In the present study, cavitation is considered to form in regions where the vapor volume fraction exceeds 50%. The shape of the supercavity is determined by extracting the volume where the vapor volume fraction is greater than 0.5. The maximum horizontal length and maximum vertical length of the extracted supercavity shape are considered as the cavitation length and maximum cavitation diameter in the current study. The non-dimensional length of the supercavity, calculated as $\tilde{L} = L/d_c$, where L is the supercavity length, and d_c is the cavitator's diameter, is compared for each case as shown in Fig 4.

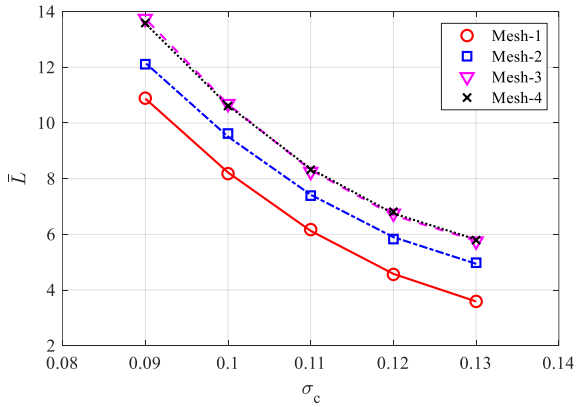

Fig. 4 Variation of non-dimensional cavitation length ($\tilde{L}$) with cavitation number (σ_c) for various meshes

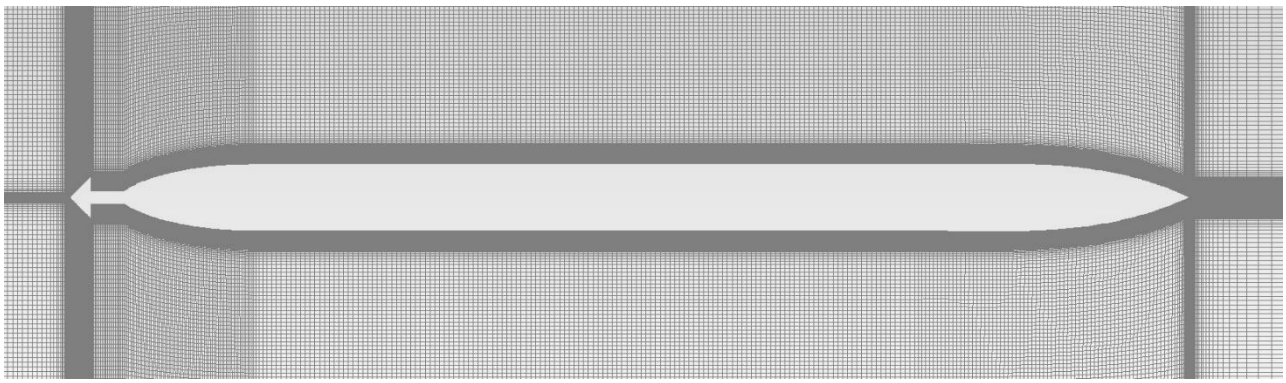

Fig. 5(a) Discretization of the computational domain

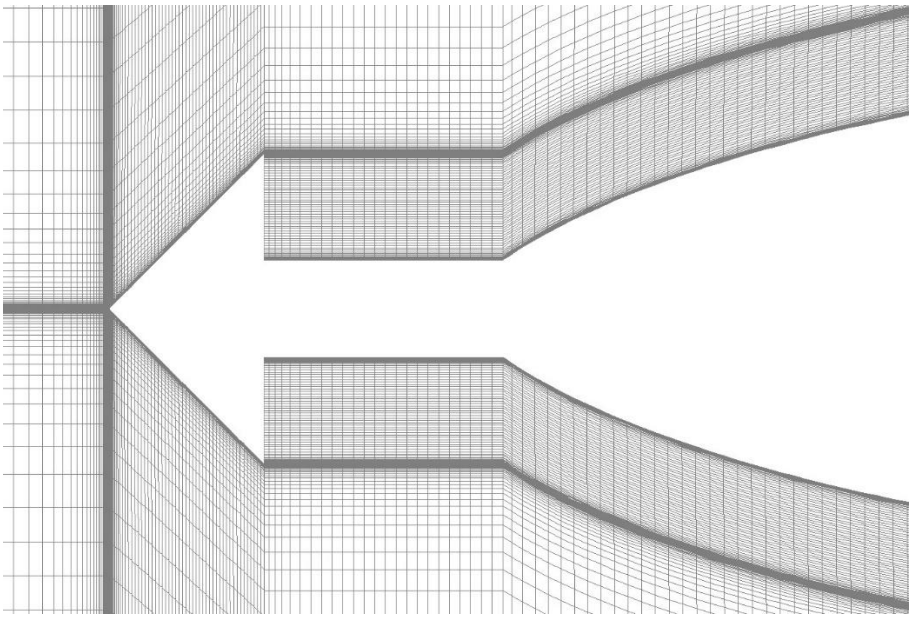

Fig. 5(b) Zoomed in view of the mesh near the cavitator

It is observed that the value of $\tilde{L}$ is changing with the number of elements for Mesh-1 and Mesh-2. However, the corresponding value remains approximately the same for Mesh-3 and Mesh-4 for all cavitation numbers. Therefore, Mesh-3, which consists of about 80,000 elements, is considered for discretizing the fluid domains of all the simulations discussed in this paper, as shown in Fig 5a.

The first cell's size is determined based on the Reynolds number range. The smallest element size which is placed on the surface of the solid object corresponds to a y+ of 40, which is outside the viscous sublayer. The wall function is employed to determine the properties within the viscous sublayer. A growth factor of 1.2 is used to generate coarser grid away from the surface. Figure 5(b) shows the zoomed-in view of the mesh near the cavitator surface

2.3 Computational Setup

In the present investigation, the computations are carried out on ANSYS fluent software. The simulations are performed using the 2D steady axisymmetric model. The current computation relies on the pressure-based algorithm's solution of the Reynolds-Averaged Navier-Stokes (RANS) equation. The fundamental premise of the RANS technique is that the time-averaged velocity field can effectively represent the turbulence occurring in a flow. The Reynolds stresses and turbulence intensities, which are crucial for the estimation of the rate of generation and dissipation of turbulent kinetic energy are computed using this time-averaged velocity field. The mass and momentum governing equation of RANS can be written as:

$$\partial\rho/\partial t + \nabla(\rho V) = 0 \tag{3}$$

$$(\partial(\rho V))/\partial t + \nabla(\rho U.U) = -\nabla p + \nabla\tau + F \tag{4}$$

where τ is Newtonian viscous stress tensor and F is body forces acting on the flow. A coupled scheme is used for the coupling of the velocity and pressure terms and the least squares cell-based approach is used to evaluate the gradients.

The primary and secondary phase materials for present computations are seawater and water vapour, respectively; with their properties as defined in Table 2. To replicate results at a depth of 10 metres, simulations are performed at an operating pressure and temperature of 201681 *Pa* and *298 K* respectively. Velocity inlet and

Table 2 Properties of seawater used in the present computation

Property	Value
Density (ρ)	$1023\ kg/m^3$
Dynamic Viscosity (μ)	$9.2\ X\ 10^{-4}\ kg/ms$
Saturation Pressure	$3494\ Pa$
Specific Heat (c_p)	$4010\ J/kgK$

pressure outlet are the respective boundary condition types for the inlet and outlet. The flow velocities employed for the simulations range between 47.5 m/s to 60 m/s which corresponds to cavitation numbers of 0.13 to 0.09.

To take into account the dynamics of multiphase flow, the VOF equations are solved using an implicit volume fraction formulation. The VOF approach defines a scalar field that represents the fraction of each phase present at any given location, which is further used to determine the interface boundary. The following is an expression for the volume fraction equation for the liquid and vapour phases:

$$(\partial\alpha_l)/\partial t + \nabla.(\alpha_l U) = (\dot{m}/\rho_l) \quad (5)$$

$$(\partial\alpha_v)/\partial t + \nabla.(\alpha_v U) = (\dot{m}/\rho_v) \quad (6)$$

where α_l and α_v represents the volume fraction of the liquid and vapour phases respectively, ρ_l and ρ_v signifies the density of liquid and vapour phases respectively, $\dot{m}$ donates the mass transfer rate per unit volume between the liquid and vapour phases due to cavitation.

In the present investigation, the occurrence of the cavitation phenomenon causes the mass transfer from the liquid phase to the vapour phase. To determine the mass transfer rate between the cavitation phases, Schnerr and Sauer cavitation model (Schnerr & Sauer, 2001) is adopted. This cavitation model applies the following equations to establish a relationship between bubble growth and volume fraction change rate:

If $p > p_v$, then

$$\dot{m}^+ = C_c \frac{\rho_v \rho_l}{\rho} \alpha_v (1-\alpha_v) \frac{3}{R} \sqrt{\frac{2}{3}\frac{p-p_v}{\rho_l}} \quad (7)$$

If $p < p_v$, then

$$\dot{m}^- = C_v \frac{\rho_v \rho_l}{\rho} \alpha_v (1-\alpha_v) \frac{3}{R} \sqrt{\frac{2}{3}\frac{p-p_v}{\rho_l}} \quad (8)$$

where R is the bubble radius, p is the static pressure, p_v and ρ_l are the vapour pressure and the density of the liquid respectively, α_v is vapour volume fraction, C_c and C_v are coefficients for the cavitation model. The bubble radius (R) can be calculate using bubble number density (n) as follows:

$$R = \left[\frac{\alpha_v}{1-\alpha_v}\frac{3}{4\pi n}\right]^{1/3} \quad (9)$$

For the present study, the value of n is taken as 10^{11}, and the value of C_c and C_v are considered as 1. The cavitation properties can be influenced by the values of these parameters. However, the simulations in this study are restricted to using these parameters at a constant value.

In addition to the cavitation model, accurate turbulence modelling is also essential in the present simulations since cavitation is typically a high-turbulence phenomenon. The realisable *k-ε* model is utilized in the present research to estimate the turbulence effect outside the viscous sublayer. The wall function is used to approximate the turbulence characteristics within the viscous sublayer. According to the *k-ε* turbulence model, turbulence mainly depends on turbulence kinetic energy (k) and dissipation rate (ε). The model estimates the impacts of turbulence on the mean flow and solves for the time evolution of these two turbulence characteristics. However, the standard *k- ε* turbulence model has certain limitations, such as sometimes producing turbulence quantities with unphysically negative values. The realisable *k-ε* model, on the other hand, includes a correction term to ensure that the turbulence dissipation rate remains positive. The accuracy of turbulence predictions improves with the implementation of this correction term. The transport equations for the realizable *k-ε* model are given below:

$$\frac{\partial}{\partial t}(\rho k) + \frac{\partial}{\partial x_j}(\rho k u_j) = \frac{\partial}{\partial x_j}\left[\left(\mu + \frac{\mu_t}{\sigma_k}\right)\frac{\partial k}{\partial x_j}\right] + G_k + G_b - \rho\varepsilon - Y_m + S_k \quad (10)$$

$$\frac{\partial}{\partial t}(\rho \varepsilon) + \frac{\partial}{\partial x_j}(\rho \varepsilon u_j) = \frac{\partial}{\partial x_j}\left[\left(\mu + \frac{\mu_t}{\sigma_\varepsilon}\right)\frac{\partial \varepsilon}{\partial x_j}\right] + \rho C_1 S_\varepsilon - \rho C_2 \frac{\varepsilon^2}{k+\sqrt{(\vartheta\varepsilon)}} + C_{1\varepsilon}\frac{\varepsilon}{k}C_{3\varepsilon}G_b + S_\varepsilon \quad (11)$$

where G_k, G_b denoted the generation of turbulence kinetic energy due to the mean velocity gradients and buoyancy respectively. Y_m denotes the contribution of the fluctuating dilatation in compressible turbulence to the overall dissipation rate, σ_k and σ_ε are turbulent Prandtl numbers for k and ε respectively. S_k and S_ε are the source terms for k and ε respectively.

2.4 Validation of Numerical Model

The accuracy of the numerical model utilised in the present study is validated by comparing the results against the experimental work of Waid (1957). The study reported the supercavity half-length and maximum diameter at various flow conditions. The experiments were conducted on a disc cavitator with a diameter of 25.4 mm at various cavitation number. The half-length and maximum diameter of the supercavity is transformed into a non-dimensional form by dividing it by the cavitator diameter. The validation procedure entails comparing the non-dimensional half-length and maximum diameter of the supercavity for various cavitation numbers. Figure 6(a) shows the comparison of non-dimensional half-length, and Fig. 6(b) represents the comparison of non-dimensional maximum diameter of the supercavity. The experimental data and computational data show good agreement, with an RMSE value of 4.62% for half-length and 4.01% for maximum diameter of the supercavity.

3. RESULTS AND DISCUSSION

The data obtained from the simulations is analysed to comprehend the flow pattern, extract the supercavity geometry, and estimate the skin friction and

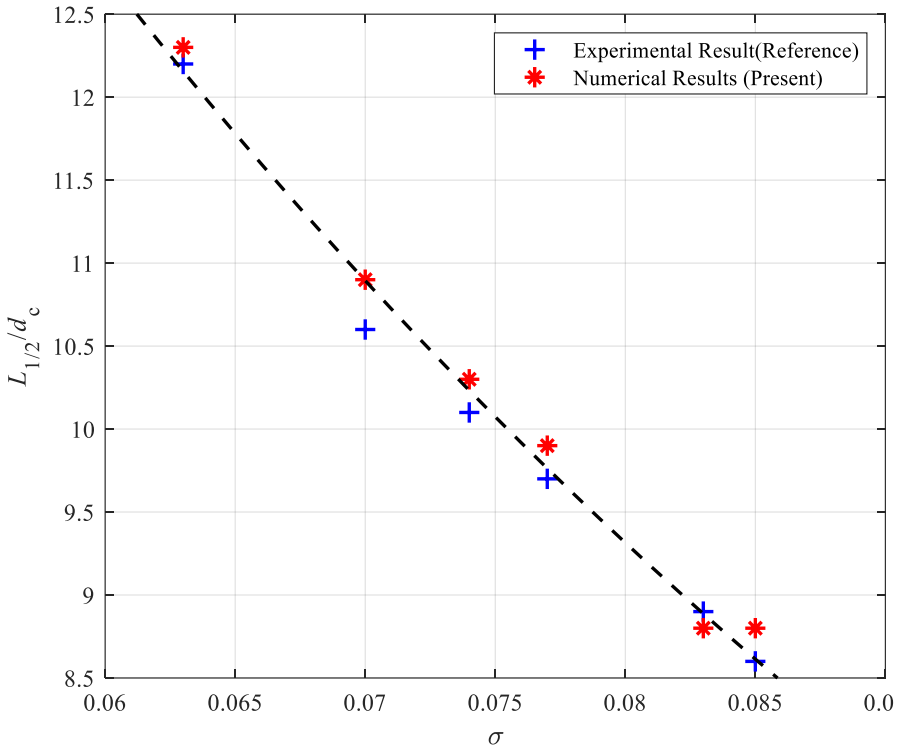

(a)

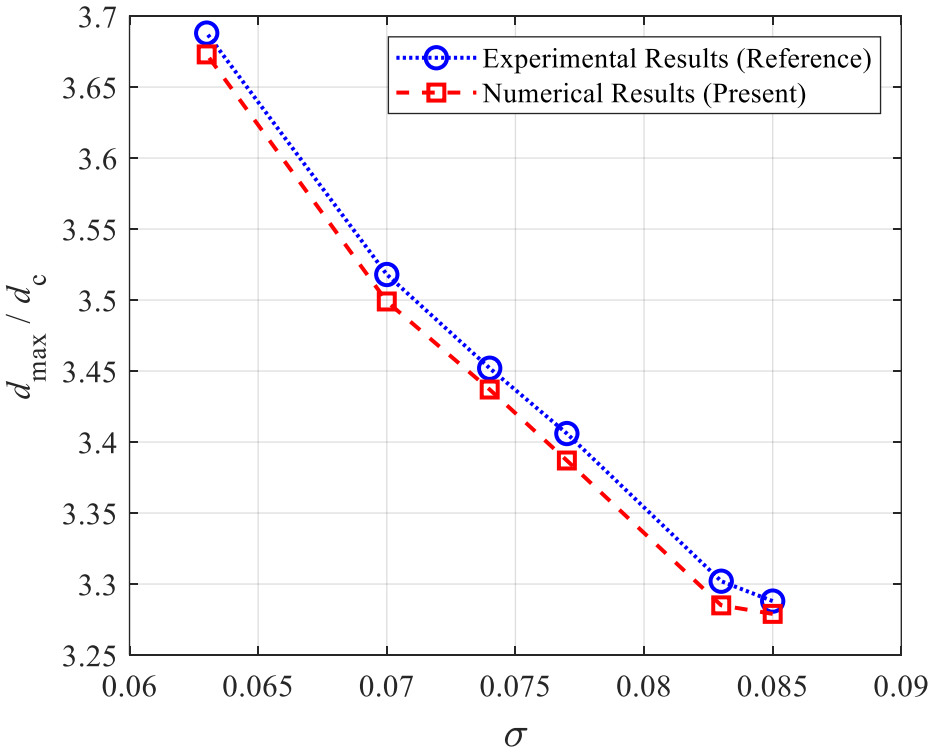

(b)

Fig. 6 Comparison of (a) Non-dimensional half-length, and (b) Non-dimensional maximum diameter of the supercavity at various cavitation number obtained from computational results from present study with the experimental result reported by Waid (1957). The dotted line represents the quadratic polynomial curve fit for the computational data in the Fig. 6a

pressure drag offered by the cavitator. Subsection 3.1 employs graphical representations to elucidate the flow patterns and associated behaviours. Subsections 3.2 and 3.3 focus on the geometrical attributes of the supercavity for various cavitators under varying cavitation numbers. Furthermore, Sections 3.4 and 3.5 respectively delve into the characteristics of skin-friction drag and pressure drag for each cavitator shape. In Section 3.6, the selection criteria for a cavitator are succinctly outlined, with a particular emphasis on its impact on the overall drag.

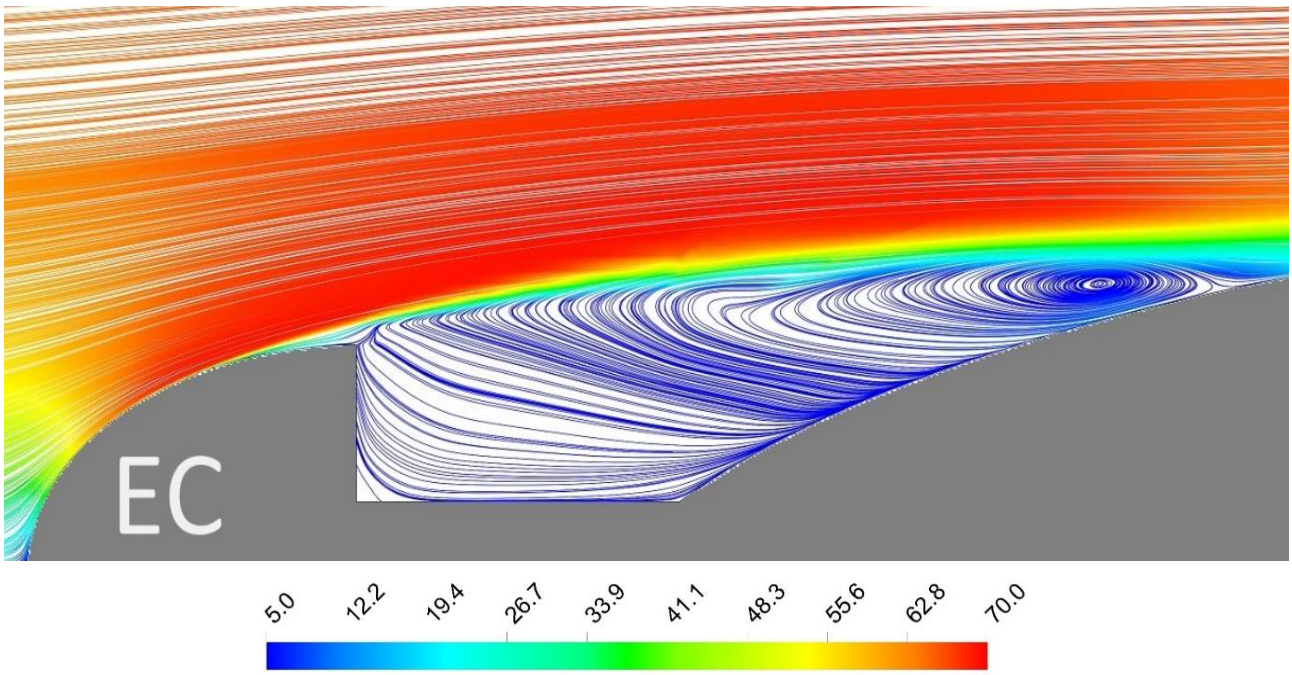

Fig. 7 Streamlines coloured by velocity magnitude over EC cavitators, Freestream flow is from left to right

3.1 Flow Patterns

To comprehend the flow patterns better, streamlines coloured by velocity magnitudes are drawn over the cavitator in Fig. 7. The pattern of the streamlines clearly suggests that the cavitator deflected the flow of seawater away from the torpedo, creating a region of low pressure adjacent to the torpedo's surface. Water starts converting into vapour phase owing to the low ambient static pressure. Since there is an adverse pressure gradient, the vapour tends to migrate upstream and generate a reverse flow. The entire process results in the formation of a recirculating zone of water vapour inside the supercavity. It was noticed that, when the supercavity length is smaller than the nose cone of the torpedo, a single recirculating zone of water vapour is formed just behind the cavitator and extended up to the cavity closure. However, when the supercavity length is larger than the torpedo's nose cone, two recirculating zones are observed. The first recirculating zone forms immediately following the cavitator whereas, the second is observed at supercavity closure. The vapour exits from the first recirculating zone and follows the flow downstream until it reaches the second recirculation zone at the supercavity closure. A new recirculating zone arises at the cavity closure as a result of high pressure at the cavity closure forcing the vapour to start moving upstream once again.

3.2 Supercavity Size

The size of the supercavity is crucial in determining the amount of friction drag that will be applied to the torpedo's body. Therefore, it is imperative to design a cavitator that can produce a supercavity to span the maximum possible torpedo surface area. The formation process of the supercavity is an unsteady phenomenon and the size of supercavity changes with time. As the simulations are conducted under the steady state assumption, the evolution of supercavity size is not reported in this study. Figure 8 shows the volume fraction of seawater that depicts the fully developed supercavity shape for various cavitators at fixed cavitation number. The contours are arranged in decreasing order of the supercavity size and clearly demonstrate that the disc cavitator (DC) can generate the largest supercavity, followed by the conical cavitator (CC-120), truncated cone cavitator (TC-16), spherical cavitator (SC), parabolic cavitator (PC), Myring cavitators (MC-1.5) and the elliptical cavitator (EC). The flow around the cavitator undergoes a localised contraction region, leading to a reduction in the local static pressure to ranges comparable to the vapour pressure of the liquid. This process induces the vaporisation of the water, resulting in the subsequent creation of the supercavity.

The observations indicate that the size of the supercavity produced is dictated by the ability of the cavitator to divert the flow in the radially outward direction. The length of the supercavity depends on the balance between two energies: the energy of expansion and the energy of contraction. A higher energy of expansion results in the formation of a larger supercavity. Thus, a cavitator with a greater ability to divert the flow radially away from itself has a higher value of the radial component of velocity. As a result, the flow past the cavitator has a high kinetic energy of expansion, which, in turn, leads to the formation of a larger supercavity.

It is also observed that for conical cavitators (CC), the length of the supercavity decreases with a decrease in the cone angle i.e., CC-120 produces the larger supercavity followed by CC-90 and CC-60 as shown in Fig. 9. The CC-120 cavitator deflects the flow in a radial outward direction at a higher angle as compared to the other two configurations, leading to the formation of a longer supercavity. This observation aligns with the previously suggested explanation for the size of the supercavity.

Fig. 8 Contour of volume fraction of seawater at σ_c of 0.09 for various cavitators: a) Without cavitator, b) DC, c) CC–120, d)TC-16, e) SC, f) PC g) MC-1.5, and h) EC

In the case of truncated cone cavitators (TC), the size of the supercavity reduces with an increase in a/b ratio, which means that TC-16 yields the largest supercavity, whereas TC-48 yields the smallest supercavity as shown in Fig. 10. This occurrence can be attributed to the fact that a smaller *a/b* ratio yields a greater flow deflection angle, hence causing formation of a larger supercavity.

For the Myring cavitator (MC), it was observed that MC-1 forms the longest supercavity, followed by MC-1.5 and MC-2 as shown in Fig. 11. It is noteworthy that the length of the supercavity decreases with an increase in the value of *n*, which represents the increase in the bluntness of the cavitator for fixed cavitator diameter and length. Among the three different configurations, MC-1 is the least blunt, resulting in the highest flow deflection angle along its outer periphery and thus generating to a bigger supercavity. In contrast, the periphery of MC-2 exhibits a near-parallel alignment with the direction of the freestream velocity.

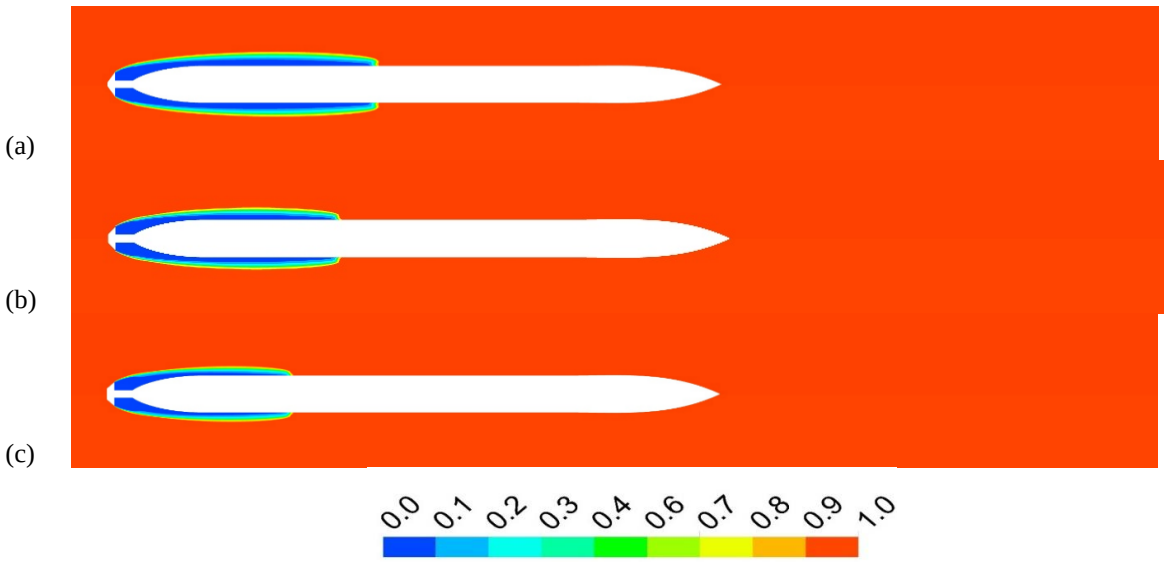

Fig. 10 Contour of volume fraction of seawater at σ_c of 0.09 for various configurations of tapered cone cavitator (a) TC-16, (b) TC-32 and (c) TC-48

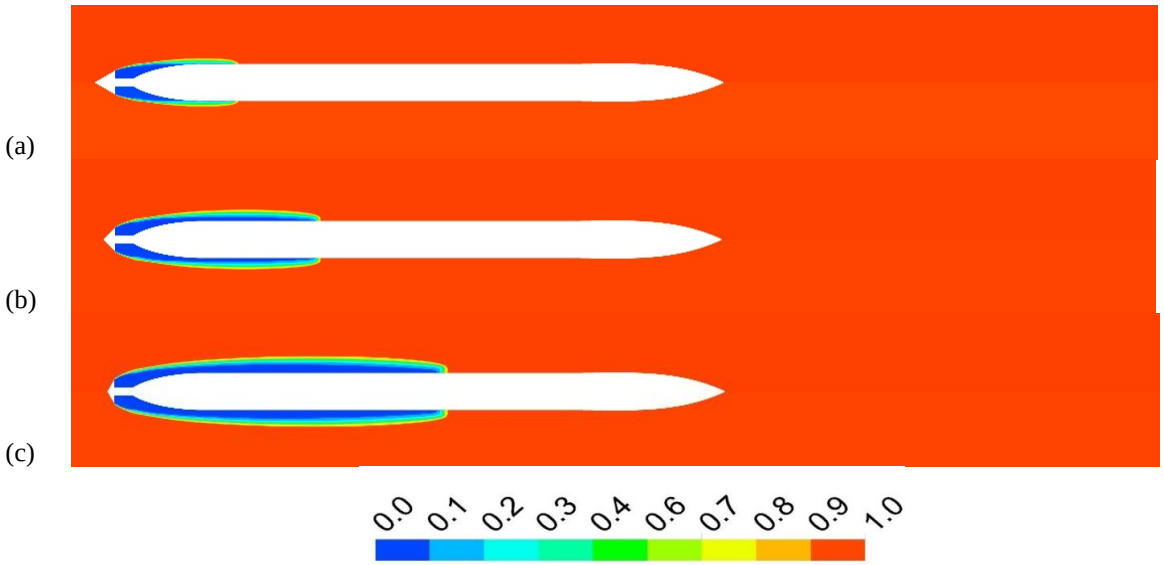

Fig. 9 Contour of volume fraction of seawater at σ_c of 0.09 for various configurations of conical cavitator (a) CC-60, (b) CC-90 and (c) CC-120

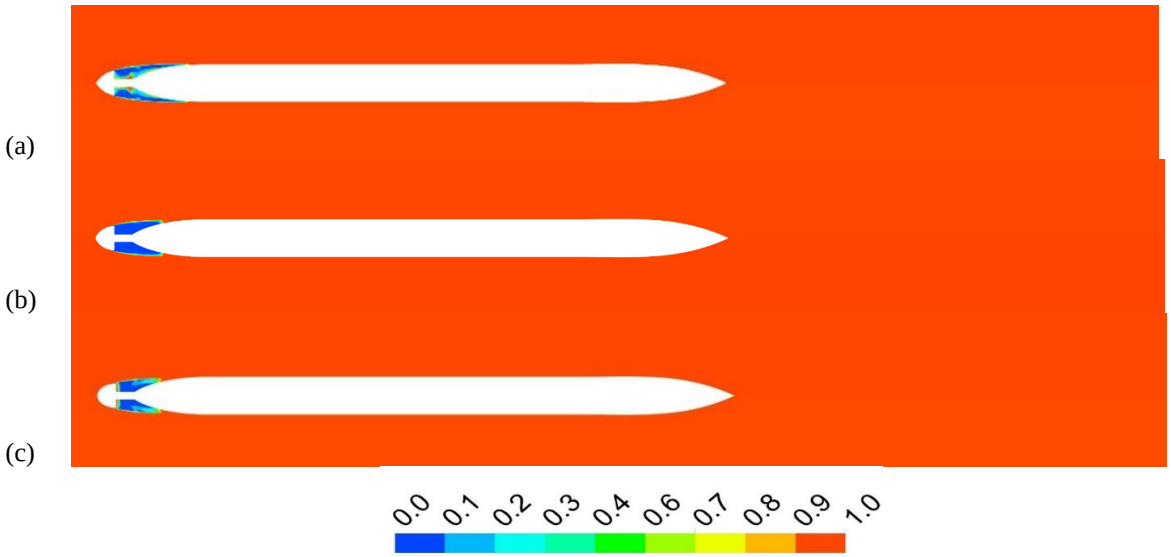

Fig. 11 Contour of volume fraction of seawater at σ_c of 0.09 for various configurations of Myring cavitator (a) MC-1, (b) MC-1.5 and (c) MC-2

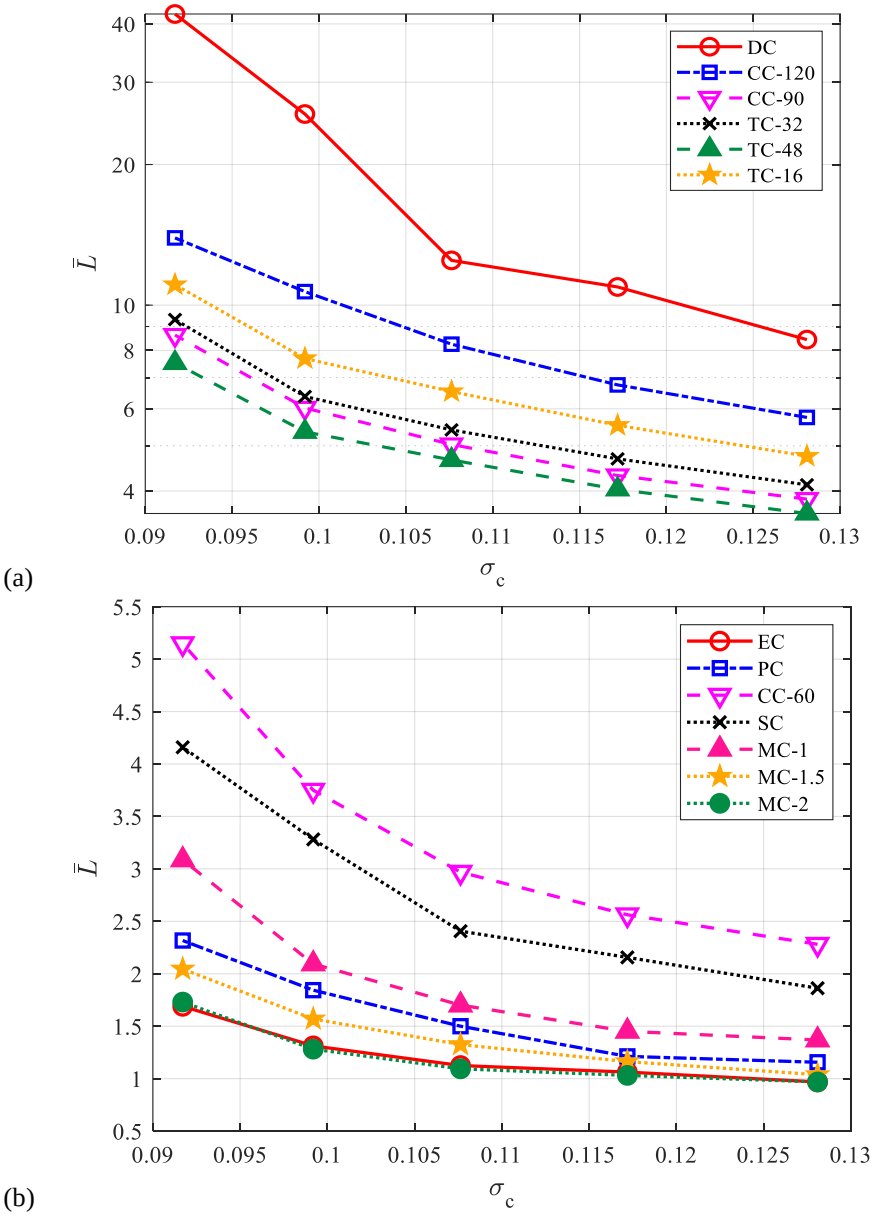

Fig. 12 Variation of non-dimensional length of the supercavity at various cavitation number for (a) the cavitators producing relatively large supercavities, and (b) those producing smaller supercavities

3.3 Cavitator's performance Evaluation at Various Cavitation Numbers (σ_c)

To effectively comprehend the performance of cavitator at varying σ_c, a plot illustrating the relationship between non-dimensional supercavity length ($\tilde{L}$) and σ_c is shown in Fig. 12, where ($\tilde{L}$) is defined as the ratio of the length of supercavity divided by cavitator diameter i.e. $\tilde{L} = L/d_c$. The length of the supercavity increases squarely in proportion to the decrease in the cavitation number. This happens because the decrease in the cavitation number represents a rise in the energy of expansion ($0.5\rho V^2$) over the energy of contraction ($p_o - p_c$).

The plot indicates that the disc cavitator can develop the largest supercavity compared to the other cavitators for all the values of σ_c, and the largest cavity was observed at σ_c of 0.09 with ($\tilde{L}$) of approximately 20. Moreover, it is noted that the order of the size of the supercavity formed by various cavitators observed at σ_c of 0.09 in the previous section is found to be the same for other values of σ_c as well. Therefore, it can be inferred that the ability of a cavitator to generate larger cavities is predominantly dependent upon the divergence angle of the flow's direction across different cavitators. It is noteworthy that each cavitator does have a different capability of producing supercavitation and must be employed according to torpedo size. For instance, CC-120 is the preferred option for torpedoes with a length that corresponds to ($\tilde{L}$) of 14, whereas TC-16 is the recommended option for torpedoes with a length corresponding to ($\tilde{L}$) of 9.

From a physical standpoint, the dynamics governing the maximal dimensions of supercavities, specifically their length and diameter, can be analytically described as dependent on the interplay between the shearing forces exerted by the fluid flow and the pressure dynamics at the cavity's closure point. This interplay is significantly

influenced by the fluid's shearing action, which seeks to extend the cavity, and the counteracting pressure forces that converge at the cavity's tail end, promoting its closure. The initial flow divergence angle at the cavitator emerges as a pivotal factor in this dynamic. A larger divergence from the horizontal flow direction correlates with an increased maximum supercavity diameter, thereby delaying the closure induced by pressure forces. This delay allows for an extended duration of shearing action on the gaseous supercavity, resulting in a more pronounced elongation.

From this perspective, the fluid impinging on the cavitator's frontal area experiences its maximum deflection in scenarios involving a disk cavitator, leading to a pronounced separation at the cavitator's edge. Consequently, the disk cavitator (DC) exhibits the longest supercavity length and largest diameter, as illustrated in Figs 12a and 13a. Conceptually, the disk cavitator can be likened to a cone cavitator with a separation angle of 180 degrees, effecting a 90-degree deflection of the incident fluid on the cavitator surface. The CC-120 follows the disk cavitator in terms of fluid deflection at the frontal area, resulting in a 60-degree flow deflection.

Further analysis of truncated cavity geometries reveals flow deflections in TC-16, TC-32, and TC-48 at approximately 54, 48, and 40 degrees respectively, whereas the CC-90's flow deflection corresponds to half its cone angle, i.e., 45 degrees. An examination of Figs 12a and 13a clearly indicates that the supercavity's length and diameter enhancements are contingent upon these deflection angles, following the sequence: DC>CC-120>TC-16>TC-32>CC-90>TC-48. Remarkably, at the lowest cavitation number, TC-48 demonstrates a length amplification ratio of about 7.9. Contrasting this, the CC-60 cavitator, with a 30-degree flow deflection compared to TC-48's 40 degrees, exhibits a significantly lower length amplification ratio of 5.2 at the lowest cavitation number.

This comparative analysis extends to various cavitator types, including SC, PC, and EC, as depicted in Figs 12b and 13b. Notably, Myring cavitators (MC-1, MC-1.5, MC-2), designed to minimize flow separation, predictably exhibit the least pronounced length and diameter enhancements, underscoring the critical influence of fluid deflection dynamics on supercavity dimensions. It is also noteworthy that when selecting the cavitator, pressure drag must also be taken into consideration in addition to the supercavity size, which is discussed in the following section.

A similar limitation on the torpedo diameter is also applicable, and thus the diameter of the torpedo must be decided such that the torpedo body accommodates inside the supercavity. Non-dimensional supercavity diameter ($\widetilde{D}$) is defined as the ratio of supercavity maximum diameter (d_{max}) to the cavitator diameter(d_c). Figure 13 shows the variation of ($\widetilde{D}$) with σ_c for various cavitators.

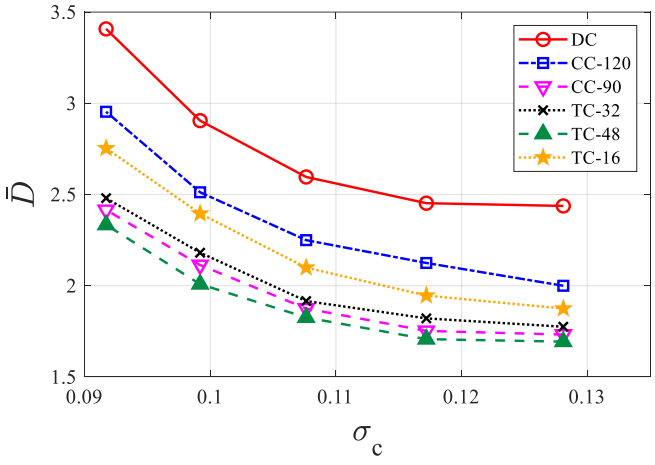

(a)

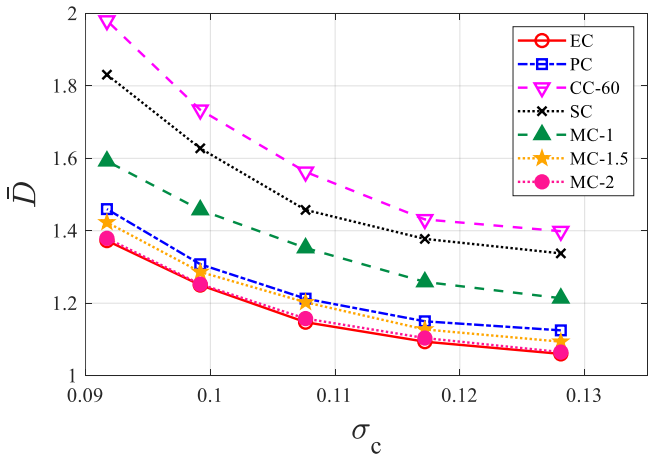

(b)

Fig. 13 Variation of non-dimensional maximum diameter of the supercavity at various cavitation number for (a) the cavitators producing relatively large supercavities, and (b) those producing smaller supercavities

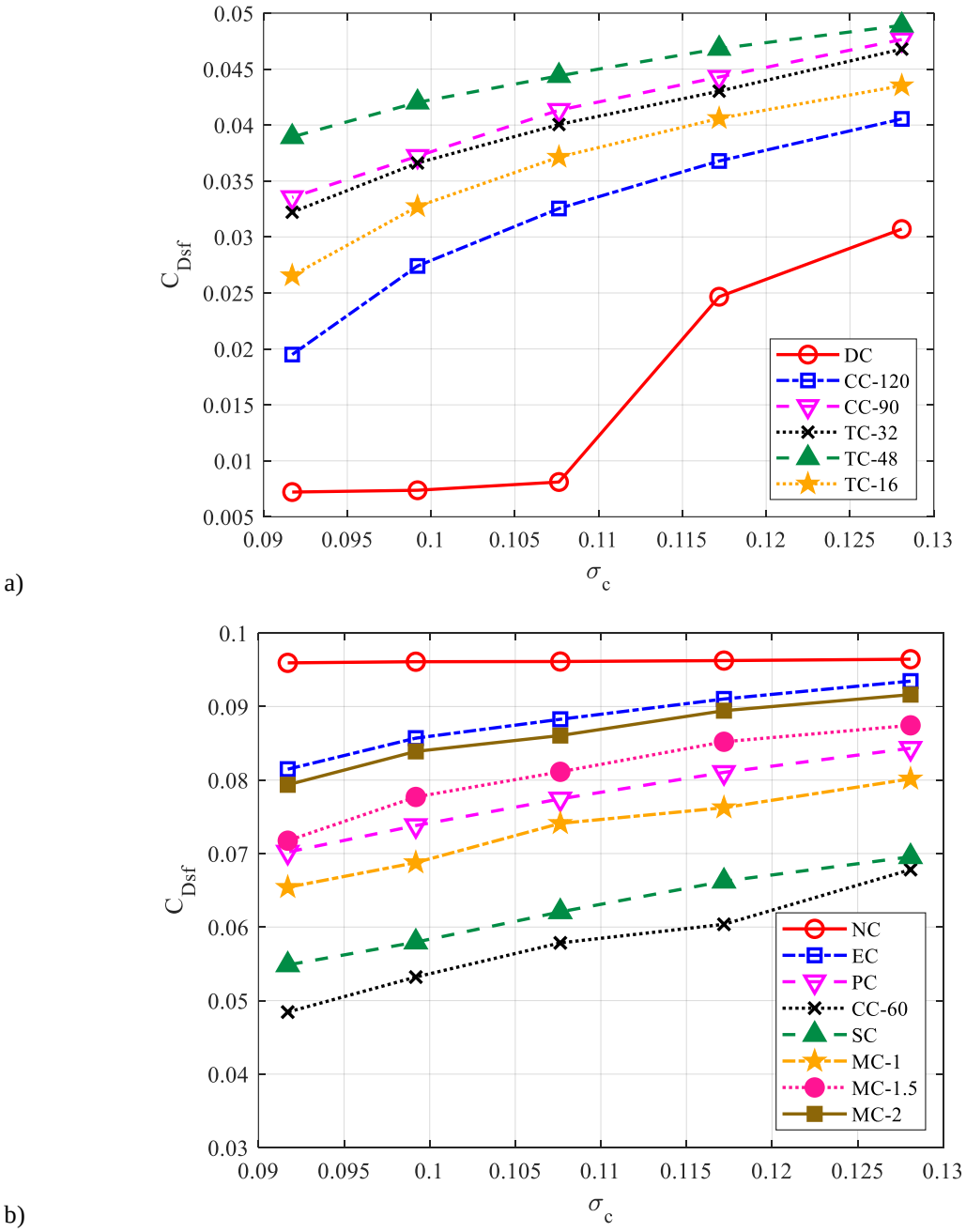

Fig. 14 Variation of skin friction drag coefficient (C_{Dsf}) with cavitation number for (a) the cavitators producing relatively large supercavities, and (b) those producing smaller supercavities

3.4 Skin Friction Drag

Once the supercavitation phenomenon creates a water vapour layer, the torpedo experiences reduced skin friction drag because the vapour layer reduces the contact area between the torpedo's surface and the water. The reduction in the amount of skin friction drag depends on the geometry of both the supercavity as well as the torpedo. The data presented in this section pertain to a heavy-weight torpedo with a diameter of 800 millimetres and a length of 8 metres. The plot shown in Fig. 14 illustrates the variation of the coefficient of skin friction drag at various cavitation numbers for different cavitators. It is apparent that the majority of the cavitator significantly decreased the skin friction drag as compared to the case without cavitator.

When considering a torpedo without a cavitator, the coefficient for skin friction drag is approximately 0.095 and maintains a relatively constant value, even when the cavitation number changes. On the other hand, when cavitators are incorporated, the coefficient for skin friction drag decreases as the cavitation number decreases due to the expansion of the supercavity. In the case of a disc cavitator, the coefficient for skin friction drag initially experiences a reduction, but subsequently stabilizes almost entirely after reaching a cavitation number of 0.11. This is because once the cavitation number reaches 0.11, the supercavity has enveloped the entire torpedo, resulting in minimal observable drag reduction despite the increase in supercavity size. The most significant decrease in skin friction drag occurs with the implementation of a disc cavitator, achieving an approximate reduction of 92%.

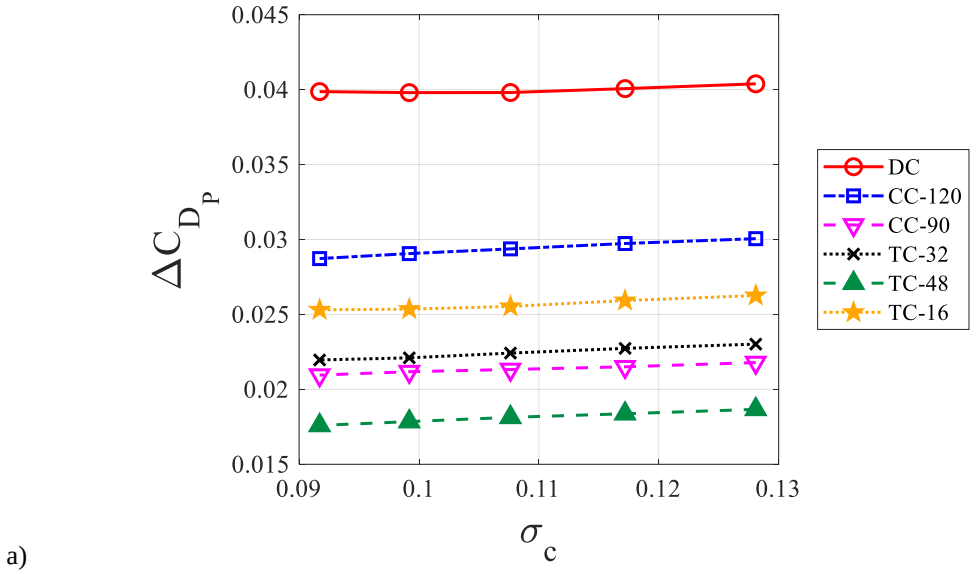

a)

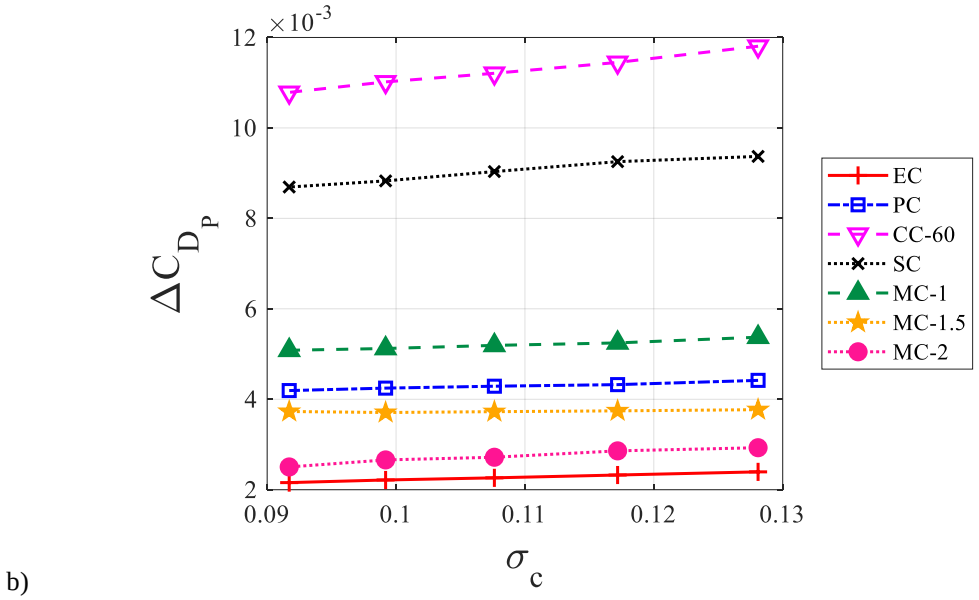

b)

Fig. 15 Change in pressure drag coefficient (C_{Dp}) at various cavitation number σ_c due to addition of (a) the cavitators producing relatively large supercavities, and (b) those producing smaller supercavities

Following closely is the CC-120 cavitator, which achieves a reduction of around 79%.

Notably, however, even though the supercavity formed by the disc cavitator at a cavitation number of 0.09 is almost 1.43 times larger than that created by the CC-120 cavitator, the percentage difference in the reduction of skin friction drag is merely 13%. This happened because the supercavity generated by the disc cavitator extends beyond the torpedo body, and the trailing portion of this supercavity does not contribute to the reduction in skin friction drag. Therefore, it is crucial to select a cavitator that produces a supercavity just large enough to surround the torpedo body.

3.5 Pressure Drag Due to Cavitator

Although the integration of the cavitator on the torpedo nose reduces the skin friction drag but it is also associated with a disadvantage of additional pressure drag offered by the cavitator. Figure 15 shows the change in pressure drag coefficient due to the addition of each cavitator at different σ_c. The plot indicates that the cavitators that produce large supercavity also provide high pressure drag. The reason for this finding can be attributed to the fact that cavitators with higher flow deflection angles exhibit larger stagnation regions. As a result, the front surface of the cavitator experiences higher pressure, leading to a correspondingly greater amount of pressure drag. For instance, a disc cavitator, due to its high flow deflection angle, has the largest stagnation zone; consequently, it is subject to the highest amount of pressure drag.

3.6 Selection of a Cavitator: Comprehensive Analysis of Overall Drag

The choice of a cavitator is determined based on the reduction in the overall drag coefficient resulting from its deployment as compared to the case when no cavitator is employed (NC). Therefore, it is necessary to take into consideration both the reduction in skin-friction drag

Table 3 Comparison of various drag coefficients for DC, CC-120 and TC-16 cavitator with respect to no cavitators (NC)

Cavitator	Reduction in skin-friction drag coefficient	Increase in pressure drag coefficient	Net reduction in overall drag coefficient
Disc	0.0887	0.0399	0.0488
CC-120	0.0765	0.0287	0.0478
TC-16	0.0694	0.0253	0.0441

(which depends on the supercavity and torpedo size) and the increase in pressure drag when identifying the best-suited cavitator shape for a particular torpedo. Table 3 presents a comparison of the drag coefficients of the three cavitator types: DC, CC-120, and TC-16 at cavitation number of 0.09 with respect to NC scenario. Other cavitators are not included in this evaluation due to their limited ability to generate a supercavity in comparison to the length of the torpedo under consideration, resulting in minimal reduction in skin friction drag. It can be deduced from the data that the disc cavitator is the most suitable choice for the heavyweight torpedo under investigation.

Nevertheless, the installation of a disc cavitator on a smaller-sized torpedo may lead to an increase in overall drag. This is due to the fact that the reduction in skin friction drag is not as significant as the substantial increase in pressure drag. Consequently, other cavitators have the potential to outperform the disc cavitator. For example, when the length of the torpedo is 10 times the diameter of the cavitator, DC, CC-120, and TC-16 cavitators can create a supercavity at a cavitation number of 0.09 that is capable of fully enclosing the torpedo while maintaining a similar level of skin friction drag. As a result, the cavitator with the lowest pressure drag, TC-16 in this scenario, will result in the least overall drag. In a similar vein, the CC-60, SC, and MC-1 cavitators are considered advantageous when the length of the torpedo is 5, 4, and 3 times the diameter of the cavitator, respectively. In summary, it can be inferred that several key aspects, such as torpedo design, cavitation number, supercavity geometry, and pressure drag on the cavitator, play a vital role in determining the most appropriate cavitator for a torpedo.

4. CONCLUSION

In the present work, simulations are carried out on thirteen different cavitators, covering a range of cavitation number ranges from 0.09 to 0.13. Various characteristics, including supercavity geometrical parameters, the skin friction drag coefficient, and changes in the pressure drag coefficient, are considered. The study demonstrates that the cavitator's ability to enhance the energy of expansion ($1/2\,\rho V^2$) by deflecting the flow radially outward allows it to generate a supercavity. The numerical results reveal that the most expansive supercavity is generated by the disc cavitator (DC), followed by the conical cavitator (CC), truncated cone cavitator (TC), spherical cavitator (SC), parabolic cavitator (PC), Myring cavitators (MC), and the elliptical cavitator (EC). The findings indicate that the dimensions of the supercavity are significantly influenced by the angle at which the flow is deflected by the cavitator. It should be noted that the size of the supercavity increases squarely in proportion to the decrease in the cavitation number for all cavitator shapes. However, the ability of the cavitator to produce a large supercavity depends solely on its geometrical shape at all the cavitation numbers considered in this study.

The reduction in the skin friction drag coefficient depends on the area of the torpedo's body that can be accommodated within the supercavity. During cavitator selection, a judicious choice pertains to the cavitator's capacity to produce a sufficiently capacious supercavity to encapsulate the torpedo. Additionally, in cases where the supercavity's dimensions exceed the torpedo's body, the coefficient of skin friction drag remains relatively constant, even as the supercavity expands. Despite the advantage conferred by diminished skin friction drag, the incorporation of a cavitator introduces the concomitant drawback of supplementary pressure drag. It is noteworthy that increases in the coefficient of pressure drag are particularly higher for cavitators generating larger supercavities. The reason for this behaviour is that a cavitator with a high flow deflection angle also encounters a larger stagnation region, resulting in higher pressure drag.

Thus, the nuanced interplay between changes in skin friction and pressure drag requires meticulous consideration in the cavitator selection process. The selection of a cavitator that generates a supercavity of dimensions just large enough to envelop the entire torpedo is desirable, as smaller supercavities induce escalations in skin friction drag, whereas larger supercavities prompt an increase in pressure drag. Ultimately, this investigation culminates in the assertion that the optimal cavitator choice for a given torpedo depends upon a composite evaluation of multiple factors, including supercavity geometry, torpedo geometry, reductions in skin friction drag, increments in pressure drag, and the range of operating cavitation numbers. It is also noteworthy that the angle of attack of the cavitator will also significantly affect the cavitation properties and can therefore be explored in future studies.

CONFLICT OF INTEREST

The author declares that there is no conflict of financial or non-financial interest to disclose.

AUTHORS CONTRIBUTION

K. Gaurav: Data curation, Methodology, Investigation, Software, Formal analysis, Writing – original draft; **N. Venkatesh:** Data curation, Methodology, Investigation, Software; **A. Karn:** Supervision, Writing – review & editing.

REFERENCES

Ahn, B. K., Jeong, S. W., Kim, J. H., Shao, S., Hong, J., & Arndt, R. E. A. (2017). An experimental investigation of artificial supercavitation generated by air injection behind disk-shaped cavitators. *International Journal of Naval Architecture and Ocean Engineering*, *9*(2), 227–237. https://doi.org/10.1016/j.ijnaoe.2016.10.006

Ahn, B. K., Lee, C. S., & Kim, H. T. (2010). Experimental and numerical studies on super-cavitating flow of axisymmetric cavitators. *International Journal of Naval Architecture and Ocean Engineering*, *2*(1), 39–44. https://doi.org/10.2478/IJNAOE-2013-0018

Cao, L., Karn, A., Arndt, R. E., Wang, Z., & Hong, J. (2017). Numerical investigations of pressure distribution inside a ventilated supercavity. *Journal of Fluids Engineering*, *139*(2), 021301. https://doi.org/10.1115/1.4035027

Chen, G., Sun, T., Yang, S., Miao, Z., & Tan, H. (2023). A study on the cavitating flow around an elliptical disk-shaped cavitator for non-body-of-revolution underwater vehicles. *Engineering Applications of Computational Fluid Mechanics*, *17*(1). Scopus. https://doi.org/10.1080/19942060.2022.2159882

Choi, J. H., Penmetsa, R. C., & Grandhi, R. V. (2005). Shape optimization of the cavitator for a supercavitating torpedo. *Structural and Multidisciplinary Optimization*, *29*(2), 159–167. https://doi.org/10.1007/s00158-004-0466-0

Erfanian, M. R., & Anbarsooz, M. (2018). Numerical investigation of body and hole effects on the cavitating flow behind a disk cavitator at extremely low cavitation numbers. *Applied Mathematical Modelling*, *62*, 163–180. https://doi.org/10.1016/j.apm.2018.05.026

Gaurav, K., Mittal, G., & Karn, A. (2022). On the morphology of elongated bubbles during their formation at submerged orifices. *Chemical Engineering Science*, *250*, 117395. https://doi.org/10.1016/j.ces.2021.117395

Javadpour, S. M., Farahat, S., Ajam, H., Salari, M., & Hossein Nezhad, A. (2017). Experimental and numerical study of ventilated supercavitation around a cone cavitator. *Heat and Mass Transfer*, *53*, 1491–1502. https://doi.org/10.1007/s00231-016-1893-3

Karn, A., & Rosiejka, B. (2017). Air entrainment characteristics of artificial supercavities for free and constrained closure models. *Experimental Thermal and Fluid Science*, *81*, 364–369. https://doi.org/10.1016/j.expthermflusci.2016.10.003

Karn, A., Arndt, R. E. A., & Hong, J. (2015a). Dependence of supercavity closure upon flow unsteadiness. *Experimental Thermal and Fluid Science*, *68*, 493–498. https://doi.org/10.1016/j.expthermflusci.2015.06.011

Karn, A., Arndt, R. E. A., & Hong, J. (2016a). An experimental investigation into supercavity closure mechanisms. *Journal of Fluid Mechanics*, *789*, 259–284. https://doi.org/10.1017/jfm.2015.680

Karn, A., Arndt, R. E. A., & Hong, J. (2016b). Gas entrainment behaviors in the formation and collapse of a ventilated supercavity. *Experimental Thermal and Fluid Science*, *79*, 294–300. https://doi.org/10.1016/j.expthermflusci.2016.08.003

Karn, A., Ellis, C., Hong, J., & Arndt, R. E. A. (2015b). Investigations into the turbulent bubbly wake of a ventilated hydrofoil: Moving toward improved turbine aeration techniques. *Experimental Thermal and Fluid Science*, *64*, 186–195. https://doi.org/10.1016/j.expthermflusci.2014.12.011

Kosel, J., Šuštaršič, M., Petkovšek, M., Zupanc, M., Sežun, M., & Dular, M. (2020). Application of (super) cavitation for the recycling of process waters in paper producing industry. *Ultrasonics Sonochemistry*, *64*, 105002. https://doi.org/10.1016/j.ultsonch.2020.105002

Likhachev, D. S., Li, F., & Kulagin, V. A. (2014). Experimental study on the performance of a rotational supercavitating evaporator for desalination. *Science China Technological Sciences*, *57*(11), 2115–2130. https://doi.org/10.1007/s11431-014-5631-0

Moghimi, M., Nouri, N. M., & Molavi, E. (2017). Experimental investigation on supercavitating flow over parabolic cavitators. *Journal of Applied Fluid Mechanics*, *10*(1), 95–102. https://doi.org/10.18869/acadpub.jafm.73.238.26678

Mokhtarzadeh, H., Balas, G., & Arndt, R. (2012). Effect of cavitator on supercavitating vehicle dynamics. *IEEE Journal of Oceanic Engineering*, *37*(2), 156–165. https://doi.org/10.1109/JOE.2011.2177689

Myring, D. F. (1976). theoretical study of body drag in subcritical axisymmetric flow. *Aeronautical Quarterly*, *27*(3), 186–194. Scopus. https://doi.org/10.1017/S000192590000768X

Nesteruk, I. (2012). *Supercavitation: Advances and Perspectives A collection dedicated to the 70th jubilee of Yu.N. Savchenko*. Springer Science & Business Media. https://www.google.co.in/books/edition/Supercavitation/8n2VdOG9Ll0C?hl=en

Newman, J. N. (2018). *Marine Hydrodynamics*. The MIT Press. https://library.oapen.org/handle/20.500.12657/26039

Oba, R., Ikohagi, T., & Yasu, S. (1980). Supercavitating cavity observations by means of laser velocimeter. *Journal of Fluids Engineering*, *102*(4), 433–438. https://doi.org/10.1115/1.3240716

Park, S., & Rhee, S. H. (2012). Computational analysis of turbulent super-cavitating flow around a two-dimensional wedge-shaped cavitator geometry. *Computers & Fluids*, *70*, 73–85. https://doi.org/10.1016/j.compfluid.2012.09.012

Rajkumar, R., Gaurav, K., Karn, A., Kumar, V., & Shukla, H. (2023). Numerical investigation of the effect of liquid temperature on supercavitation. In S. Narendranth, P. G. Mukunda & U. K. Saha (Eds.), *Recent Advances in Mechanical Engineering* (pp. 19–27). Springer Nature. https://doi.org/10.1007/978-981-19-1388-4_2

Sarc, A., Kosel, J., Stopar, D., Oder, M., & Dular, M. (2018). Removal of bacteria legionella pneumophila, escherichia coli, and bacillus subtilis by (super) cavitation. *Ultrasonics Sonochemistry*, *42*, 228–236. https://doi.org/10.1016/j.ultsonch.2017.11.004

Savchenko, Y. (2001). Supercavitation-problems and perspectives. https://resolver.caltech.edu/CAV2001:lecture.003

Schmid, A. (2009). A new aeration technology using "Supercavitation." *Recent Patents on Chemical Engineering*, *2*(3), 176–180. https://shorturl.at/NtCXl

Schnerr, G. H., & Sauer, J. (2001). *Physical and numerical modeling of unsteady cavitation dynamics*. Fourth International Conference on Multiphase Flow, 1. https://www.researchgate.net/publication/296196752_Physical_and_Numerical_Modeling_of_Unsteady_Cavitation_Dynamics

Semenenko, V. N. (2001). *Artificial supercavitation. Physics and calculation*. https://apps.dtic.mil/sti/tr/pdf/ADP012080.pdf

Shao, S., Balakrishna, A., Yoon, K., Li, J., Liu, Y., & Hong, J. (2020). Effect of mounting strut and cavitator shape on the ventilation demand for ventilated supercavitation. *Experimental Thermal and Fluid Science*, *118*. Scopus. https://doi.org/10.1016/j.expthermflusci.2020.110173

Shao, S., Karn, A., Ahn, B.-K., Arndt, R. E. A., & Hong, J. (2017). A comparative study of natural and ventilated supercavitation across two closed-wall water tunnel facilities. *Experimental Thermal and Fluid Science*, *88*, 519–529. https://doi.org/10.1016/j.expthermflusci.2017.07.005

Shi, H. H., Itoh, M., & Takami, T. (2000). Optical observation of the supercavitation induced by high-speed water entry. *Journal of Fluids Engineering*, *122*(4), 806–810. https://doi.org/10.1115/1.1310575

Waid, R. L. (1957). *Cavity shapes for circular disks at angles of attack*. https://core.ac.uk/download/pdf/216213457.pdf

Xu, C., & Khoo, B. C. (2020). Dynamics of the supercavitating hydrofoil with cavitator in steady flow field. *Physics of Fluids*, *32*(12), 123307. https://doi.org/10.1063/5.0030907

Zhang, X., Wei, Y., Zhang, J., Cong, W., & Yu, K. (2007). Experimental research on the shape characters of natural and ventilated supercavitation. *Journal of Hydrodynamics, Ser. B*, *19*(5), 564–571. https://doi.org/10.1016/S1001-6058(07)60154-1